




A Microfacet-based Hair Scattering Model

W. Huang¹  and M. B. Hullin¹  and J. Hanika² 

¹University of Bonn, Germany

²Karlsruhe Institute of Technology, Germany

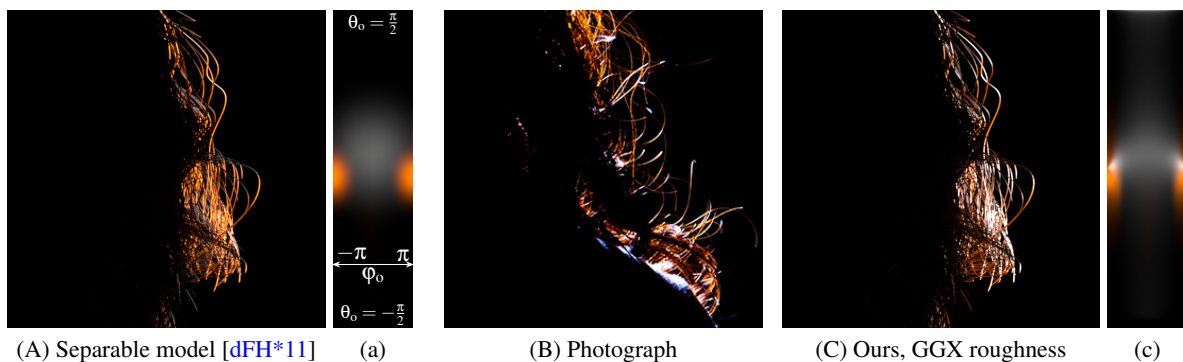


Figure 1: Detail of a backlit studio scene rendered using a state-of-the-art separable hair scattering model (A) and the proposed model (C), both compared with a photograph under similar lighting conditions (B) (© Martyn Thompson <https://photographymk.co.uk>), with visualization of the BCSDF (a,c) as plotted against θ_o/ϕ_o , illumination angle $\theta_i = 0$. The strongly focused reflection in the forward scattering direction seen in (C,c) gives rise to a glint-like appearance that the previous separable hair scattering models have been unable to capture. (Exposure of (a,c) is scaled up by 2.5 stops to improve feature visibility. (A,C) are close-up images of Fig. 13.)

Abstract

The development of scattering models and rendering algorithms for human hair remains an important area of research in computer graphics. Virtually all available models for scattering off hair or fur fibers are based on separable lobes, which bring practical advantages in importance sampling, but do not represent physically-plausible microgeometry. In this paper, we contribute the first microfacet-based hair scattering model. Based on a rough cylinder geometry with tilted cuticle scales, our far-field model is non-separable by nature, yet allows accurate importance sampling. Additional benefits include support for elliptical hair cross-sections and an analytical solution for the reflected lobe using the GGX distribution. We show that our model captures glint-like forward scattering features in the R lobe that have been observed before but not properly explained.

CCS Concepts

• *Computing methodologies* → *Reflectance modeling*;

1. Introduction

Rendering realistic hair is important for virtual creatures and humans. It has thus received attention in computer graphics literature early on [KK89]. A more detailed look at the effects contributing to the distinct look of hair established that the dielectric fiber surface reflects (R) and transmits (T) part of the light [MJC*03]. Most prominently, the scattering distribution of hair is composed of an R lobe, a TT lobe, and a TRT lobe, denoted by the type and order of interactions between the light path and the fiber surface. Hair has

slightly tilted cuticle scales on the surface, which are responsible for a shift between the direct highlight (R) and the secondary reflection (TRT). Also, light passing through the pigmented fiber picks up the distinct coloration of the material and results in the lively appearance of the two prominent highlights, R and TRT. Lobes of higher order, where the light has passed through the fiber multiple times (TRRT, ...) exist as well, but are usually weak enough to be neglected thanks to repeated absorption.

Monte Carlo path tracing of hair is hard: the size of the individual

fibers is usually small (on the order of a tenth of a millimeter), so already finding an intersection of a ray with such a sub-pixel-sized object is hard. To counter this, analytic fiber scattering models pre-integrate over the cross-section of the hair: the geometric primitive to intersect is not actually a cylinder, but a ray-facing stripe, and the curvature of the cylinder is included in the equations for the lobes. This way it is certain that all offsets from the stripe center, i.e. normals on the cylinder, are considered appropriately.

This approach poses a set of challenging mathematical problems. To make these tractable, separating the equations into a longitudinal and azimuthal factor was proposed [MJC*03]. This mathematical simplification was so successful that it can be found in the most advanced models to date. On the flip side, this artificial factorization of the scattering lobes does not have a physical motivation. Basing advanced models on this assumption has thus become increasingly hard, resulting in complicated equations which still fail to capture even simulated reference faithfully in all cases.

In parallel to this development, microfacet-based surface reflectance models have gained popularity in computer graphics and have been studied in quite some detail. We revisit fiber scattering models with this background and devise a *bidirectional curve scattering distribution function* (BCSDF) which is rooted in microfacet theory. We still intersect ray-facing stripes, but then include a cylindrical macrosurface, tilted scales as mesosurface, as well as a microsurface with Beckmann or GGX normal distribution function in our analysis. This formulation naturally includes glinty behavior at grazing angles and a non-separable shape of the lobes in longitudinal/azimuthal space. The existence of this shape has been observed before [dMH14; KM17], but could not be reproduced with a physically-based model. We show how a physically-plausible surface model simplifies working with the BCSDF: importance sampling becomes simple, we provide a closed-form solution for the GGX R lobe, and our equations naturally extend to elliptical fiber macrogeometry.

In summary, our contributions in this paper are:

- the first fiber scattering model based on physically-plausible macro-, meso-, and microgeometry,
- accurate importance sampling despite non-separable lobes,
- an analytic form of the resulting integral for the R lobe with GGX microroughness,
- a natural extension to elliptical cross-sections.

2. Background and Related Work

Light transport. Physically-based rendering has a long history [PJH18]. The most successful numerical method to solve the integrals appearing in the transport equations is Monte Carlo path tracing. Materials are included in the physical model via the *bidirectional scattering distribution function* (BSDF), which relates incoming irradiance to outgoing radiance. This function is valid on locally flat surfaces and is often derived from statistical models of the microsurface by applying a far-field assumption. Analogous to that, there is the *bidirectional curve scattering distribution function* (BCSDF) which models the same material properties assuming a ray-facing stripe as underlying geometry, i.e., it can encode the curvature of a cylinder inside it.

Fiber scattering models. Most if not all fiber scattering models in computer graphics today can be traced back to Marschner's work [MJC*03]. After intersecting a ray-facing curve primitive, the BCSDF is evaluated when connecting to the light source. To make the definition of this BCSDF tractable, they separated the model into a longitudinal (depending on θ) and an azimuthal part (depending on ϕ). These two are multiplied together to form the final lobe. In addition to that, the full model consists of multiple lobes, one for the directly reflected light (R), the light transmitting through the fiber (TT) and the lobe formed by light entering the fiber, and exiting it again after internal reflection (TRT). This scheme can be extended indefinitely, but the contribution of the higher-order lobes vanishes soon.

In Monte Carlo path tracing, importance sampling and energy conservation are important topics and have been looked into [dFH*11; CBTB16]. Also, there is an excellent implementation guide [PJH18] of Chiang's work [CBTB16]. Later, the model has been extended to structures inside the fiber and for a stochastic near- and far-field model [YTJR15; YJR17]. The importance of elliptical hair fiber cross-sections has been pointed out and a specialized azimuthal scattering function has been devised to this end [KM17]. The separable model with longitudinal/azimuthal functions has even been extended to include certain effects of diffraction [XWM*20; BP21], while still keeping the original assumption of separability. We do not consider wave-optics in this work.

The notable exception to this pattern is a paper by d'Eon et al. [dMH14], who showed that the non-separable nature of the reflectance field causes a strong, focused forward scattering effect. They conducted an offline Monte Carlo simulation of a rough dielectric cylinder, which is the underlying geometry of the Marschner model [MJC*03], and hand-tailored a non-separable model that would match their observation better. Since importance-sampling a non-separable 2D function is not trivial, they proposed an approximate way of approaching this problem.

We take their observation further and show that the underlying geometry of a rough dielectric cylinder can be traced directly using microfacet theory without the effort of separation. The resulting lobes match the Monte Carlo reference much closer than previous approaches. Since it is based on well-studied microfacet models, we can importance sample the lobes of our model exactly using standard inverse-CDF sampling.

Microfacet theory has a long history in literature, as it is relevant to antenna theory and heat transfer, with which physically-based rendering shares a great deal of theory. The surface of a material is thought of as a set of microfacets with certain reflection properties. Often they are assumed to be perfect mirrors with material specific Fresnel behavior [CT82]. The geometry of the microsurface is modeled statistically, to avoid instantiating and ray tracing a multitude of geometric primitives. Certain random distributions of the height and normals of the facets can be applied, and most often they are assumed to be uncorrelated with each other, i.e. the surface consists of disconnected, independent facets (a Smith surface [Smi67]). The foundation of modern microfacet models in computer graphics is Heitz' work [Hei14]. The generic form of a *bidirectional reflectance distribution function* (BRDF) for scattering on

flat surfaces is

$$f_r(\omega_i, \omega_o) = \frac{F(\omega_h, \omega_o)G(\omega_o, \omega_i, \omega_h)D(\omega_h)}{4|\omega_m \cdot \omega_o||\omega_m \cdot \omega_i|}. \quad (1)$$

Here, ω_i and ω_o are the incident and outgoing directions, ω_h is the half vector (or, equivalently, the micronormal), ω_m the geometric normal of the macrosurface, F is the Fresnel term, and G the combined geometric factor for shadowing and masking within the microsurface. This model only represents single scattering in the microsurface, so it fulfills energy conservation only insofar as it does not generate energy. Since it lacks multiple scattering contributions [HHdD16; LJJ*18; Tur19], it will be visibly too dark for very rough surfaces.

There has been a lot of interest in surface scattering models that exhibit off-center reflectance peaks, i.e. the mean orientation of the microfacets is not aligned with the normal of the triangle mesh. To this end, the surface orientation can be divided up in micronormal, mesonormal, and macronormal [DHI*13]. To arrive at a consistent surface model, the mesosurface has to be closed. Schüßler et al. [SHHD17] devise such a model including multiple scattering in the mesosurface for normal maps.

The case analyzed in our work is similar: the macrosurface is a cylinder, the mesosurface consists of tilted cuticle scales, and the microsurface is a Smith surface. We apply microfacet theory to this setting and arrive at a reflectance model for hair fibers, including R, TT, and TRT lobes for circular and elliptical cross-sections.

3. Model

In this section, we describe our model and its implementation details. First, we will describe the geometry and derive the basic lobe evaluation formulas in Section 3.1. Extensions to scale tilt (Section 3.2) and elliptical cross-sections (Section 3.3) follow after. Section 3.4 then summarizes aspects related to the requirements of Monte Carlo rendering system: evaluation, importance sampling, evaluation of the probability distribution function.

3.1. A Microfacet BCSDF

We model the fiber as a cylinder with microfacet surface roughness, having a radius of 1 (Fig. 2). In accordance with former fiber- and hair-models, we associate the outgoing radiance L_o with the incoming radiance L_i via the *Bidirectional Curve Scattering Distribution Function* (BCSDF) $S(\omega_i, \omega_o)$

$$L_o(\omega_o) = \int L_i(\omega_i)S(\omega_i, \omega_o) \cos \theta_i d\omega_i. \quad (2)$$

We limit our discussion to R, TT, and TRT lobes, therefore

$$S(\omega_i, \omega_o) = S_R(\omega_i, \omega_o) + S_{TT}(\omega_i, \omega_o) + S_{TRT}(\omega_i, \omega_o). \quad (3)$$

The relevant vectors to appear in the following subsections are illustrated in Fig. 3.

3.1.1. Reflection Lobe S_R

For perfectly specular microfacets, only the half-angle vector $\omega_{h1} = \widehat{\omega_i + \omega_o}$ contributes to the reflection from ω_i to ω_o . Consider a differential surface area element

$$da_{m1} = d\phi_{m1} ds \quad (4)$$

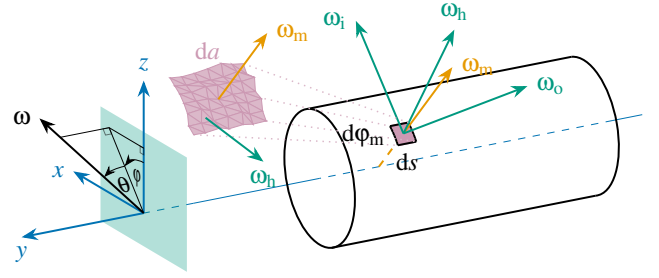


Figure 2: An illustration of the geometry of our hair scattering model. The longitudinal-azimuthal parameterization is shown on the left. The longitudinal angle θ is defined as the angle between ω and the $x-z$ plane, and the azimuthal angle ϕ is the angle between the z axis and the projection of ω onto the $x-z$ plane. da is a differential surface element with macronormal ω_m , which is composed of specular microfacets ω_h with associated normal distribution $D(\omega_h, \omega_m)$.

with the macronormal direction ω_{m1} and the differential length ds along the fiber. Such a differential surface has an associated distribution $D(\omega_{h1}, \omega_{m1})$ of micronormals ω_{h1} , which satisfies

$$\int_{\mathcal{H}^2(\omega_{m1})} D(\omega_{h1}, \omega_{m1}) |\omega_{h1} \cdot \omega_{m1}| d\omega_{h1} = 1, \quad (5)$$

where $|\cdot|$ denotes the absolute value of the dot product. The area of the differential surface element da_{h1} with micronormals ω_{h1} is

$$da_{h1} = D(\omega_{h1}, \omega_{m1}) d\omega_{h1} da_{m1}. \quad (6)$$

The differential flux $d\Phi_{h1}$ received by such microfacets is

$$d\Phi_{h1} = L_i(\omega_i) d\omega_i |\omega_i \cdot \omega_{h1}| da_{h1}. \quad (7)$$

Multiplying the Fresnel reflectance gives

$$d\Phi_o = R(\omega_{h1}, \omega_o) d\Phi_{h1}, \quad (8)$$

the differential outgoing flux from the surface element da_{m1} . The total outgoing flux is given by integrating the differential flux. Therefore, the average outgoing radiance from the fiber is

$$L_o(\omega_o) = \frac{\int d\Phi_o}{d\omega_o a_o^\perp}, \quad (9)$$

where

$$a_o^\perp = 2 \cos \theta_o ds \quad (10)$$

is the projected area of the full-width fiber in the outgoing direction. Making use of the half-angle mapping $d\omega_{h1} = \frac{d\omega_o}{4|\omega_{h1} \cdot \omega_i|}$ and combining Eqs. (4) and (6) to (10), we obtain

$$L_o(\omega_o) = \iint \frac{L_i(\omega_i) R(\omega_{h1}, \omega_o) D(\omega_{h1}, \omega_{m1}) d\phi_{m1} d\omega_i}{8 \cos \theta_o}. \quad (11)$$

Comparing Eq. (11) with Eq. (2) and adding the Smith shadowing-masking term $G_{\omega_{m1}}(\omega_i, \omega_o)$ gives the BCSDF for the R lobe

$$S_R(\omega_i, \omega_o) = \frac{R(\omega_{h1}, \omega_o)}{8 \cos \theta_o \cos \theta_i} \int D(\omega_{h1}, \omega_{m1}) G_{\omega_{m1}}(\omega_i, \omega_o) d\phi_{m1}. \quad (12)$$

Different from former fiber models [MJC*03; dFH*11; YTJR15; YJR17], we do not separate the BCSDf into longitudinal and azimuthal components; rather, we compute the half-angle vector ω_{h1} between incoming and outgoing angles, and integrate its distribution along the azimuth. Other than this integration, Eq. (12) is almost identical with the Cook-Torrance BRDF in Eq. (1), which makes sense, since we have applied the same model on a curved surface, instead of on a flat surface.

Hairs usually have low roughness values, therefore, $G \approx 1$ holds for a large range of normal directions. Interestingly, if ignoring the shadowing-masking function, an analytical solution of Eq. (12) exists for GGX roughness. The result can be found in Appendix A.

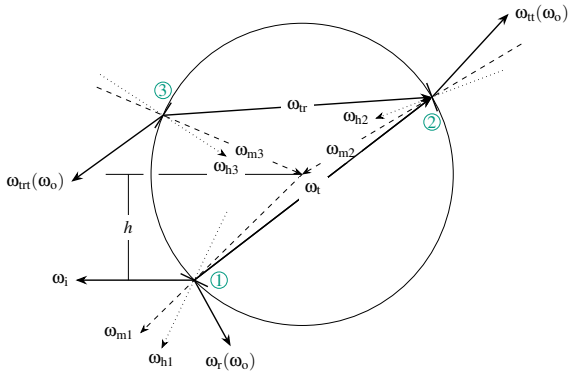


Figure 3: R , TT and TRT scattering from a circular cross-section. At each interface with macro/mesonormals ω_{mi} , $i \in 1, 2, 3$, the ray hits a microfacet (denoted with thick line segments) with normal ω_{hi} , after which it undergoes specular reflection and refraction. Note the directions the vectors are pointing to. $h \in [-1, 1]$ denotes the azimuthal offset.

3.1.2. Secondary Lobes S_{TT} and S_{TRT}

The BCSDfS for TT and TRT lobes are derived in similar ways. The differential flux transmitted through interface ① (Fig. 3) is

$$d\Phi_t = T_1 d\Phi_{h1}, \quad (13)$$

where $T_1 = 1 - R(\omega_{h1}, \omega_o)$ is the Fresnel transmittance. The corresponding radiance is

$$L_t = \frac{d\Phi_t}{d\omega_t da_t^\perp}, \quad (14)$$

with

$$da_t^\perp = |\omega_t \cdot \omega_{m1}| da_{m1} \quad (15)$$

being the projected microsurface area in the direction of ω_t . The differential flux received by microfacets with normal direction ω_{h2} is

$$d\Phi_{h2} = A_t L_t d\omega_t |\omega_t \cdot \omega_{h2}| da_{h2}. \quad (16)$$

Here we have introduced A_t as the absorption due to pigments inside the hair as the ray travels along ω_t . Two kinds of pigments are responsible for absorption inside hair: eumelanin and

pheomelanin with concentrations ρ_e and ρ_p , respectively. Let $\sigma_a = \rho_e \sigma_{a,e} + \rho_p \sigma_{a,p}$ be the absorption per unit length [DJ06], then

$$A_t = \exp\left(-\sigma_a \frac{2 \cos(\varphi_t - \varphi_{m1} + \pi)}{\cos \theta_t}\right). \quad (17)$$

Note that the path length $2 + 2 \cos(2\gamma_t)$ in the original model [MJC*03] and its derivation [dFH*11] has left out a square root when applying law of cosines and is erroneous, it should be $2 \cos \gamma_t$, as the term in Pharr's work [Pha16].

Similar to Eq. (6), the area of the surface element da_{h2} with micronormals ω_{h2} is given by

$$da_{h2} = D(\omega_{h2}, \omega_{m2}) d\omega_{h2} da_{m2}, \quad (18)$$

with

$$da_{m2} = d\varphi_{m2} ds. \quad (19)$$

Thus, the outgoing flux for the TT component is

$$d\Phi_o = T_2 d\Phi_{h2}, \quad (20)$$

with $T_2 = 1 - R(\omega_{h2}, \omega_t)$ being the Fresnel transmittance through interface ②. Note the change in relative refractive index when exiting the fiber. Further, the half vector and the outgoing direction is related by

$$\begin{aligned} d\omega_{h1} &= \frac{\eta^2}{\|\bar{\omega}_{h1}\|^2} |\omega_t \cdot \omega_{h1}| d\omega_t, \\ d\omega_{h2} &= \frac{1}{\eta^2 \|\bar{\omega}_{h2}\|^2} |\omega_t \cdot \omega_{h2}| d\omega_o, \end{aligned} \quad (21)$$

with $\bar{\omega}_{h1} = -\omega_i - \eta \omega_t$ and $\bar{\omega}_{h2} = -\omega_t + \omega_o/\eta$ being the unnormalized normal vectors and $\|\cdot\|$ their norms, and η the relative refractive index of hair with respect to air. Combining Eqs. (6), (7), (9), (10), (13) to (16) and (18) to (21), we obtain

$$\begin{aligned} L_o &= \frac{L_i}{2 \cos \theta_o} \int \frac{T_1 T_2}{\|\bar{\omega}_{h1}\|^2 \|\bar{\omega}_{h2}\|^2} |\omega_i \cdot \omega_{h1}| |\omega_t \cdot \omega_{h1}| |\omega_o \cdot \omega_{h2}| |\omega_t \cdot \omega_{h2}| \\ &\quad \iint \frac{D_1 D_2 G_1 G_2 A_t}{|\omega_t \cdot \omega_{m1}|} d\varphi_{m2} d\omega_t d\omega_i. \end{aligned} \quad (22)$$

Here we have simplified $D(\omega_{hi}, \omega_{mi})$ as D_i , and the shadowing-masking term at interface ② as G_i . Making use of $\varphi_{m1} = 2\varphi_t - \varphi_{m2}$, the BCSDf for the TRT lobe is given as

$$\begin{aligned} S_{TT}(\omega_i, \omega_o) &= \frac{1}{2 \cos \theta_o \cos \theta_i} \\ &\quad \int \frac{T_1 T_2}{\|\bar{\omega}_{h1}\|^2 \|\bar{\omega}_{h2}\|^2} |\omega_i \cdot \omega_{h1}| |\omega_t \cdot \omega_{h1}| |\omega_o \cdot \omega_{h2}| |\omega_t \cdot \omega_{h2}| \\ &\quad \int \frac{D_1 D_2 G_1 G_2 A_t}{|\omega_t \cdot \omega_{m1}|} d\varphi_{m1} d\omega_t. \end{aligned} \quad (23)$$

Repeating the above process at interface ③, we obtain the BCSDf for the TRT lobe

$$\begin{aligned} S_{TRT}(\omega_i, \omega_o) &= \frac{1}{8 \cos \theta_o \cos \theta_i} \int \frac{T_1}{\|\bar{\omega}_{h1}\|^2} |\omega_i \cdot \omega_{h1}| |\omega_t \cdot \omega_{h1}| \\ &\quad \int \frac{R_2 T_3}{\|\bar{\omega}_{h3}\|^2} |\omega_{tr} \cdot \omega_{h3}| |\omega_o \cdot \omega_{h3}| \\ &\quad \int \frac{D_1 D_2 D_3 G_1 G_2 G_3 A_t A_{tr}}{|\omega_t \cdot \omega_{m1}| |\omega_{tr} \cdot \omega_{m2}|} d\varphi_{m1} d\omega_{tr} d\omega_t, \end{aligned} \quad (24)$$

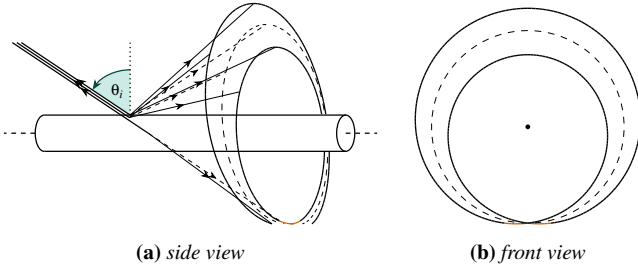


Figure 4: Parallel rays reflected off a smooth cylinder. Without cuticle scales, the reflected rays are restricted to a specular cone (dashed). In the presence of cuticle scales, the reflected rays form a conical surface but not a cone anymore (solid). We demonstrate the case for $\alpha = 4^\circ$ and $\alpha = -4^\circ$. Regions that are unreachable because of invisibility is marked red. For the purpose of illustration, the radius of the cylinder is set to zero in the front view.

with

$$A_{tr} = \exp\left(-2\sigma_a \frac{\cos(\varphi_{tr} - \varphi_{m2} + \pi)}{\cos\theta_{tr}}\right) \quad (25)$$

and making use of $\varphi_{m3} = \varphi_{m1} - 2(\varphi_t - \varphi_{tr}) + \pi$.

3.2. Scale Tilt

Hairs have tilted surface scales [MJC*03], resulting a shift of the macronormal from $\omega_m = [\sin\varphi_m, 0, \cos\varphi_m]^\top$ to the mesonormal $\omega_{m\alpha} = [\sin\varphi_m \cos\alpha, \sin\alpha, \cos\varphi_m \cos\alpha]^\top$, with α being the tilt angle. Also, additional intersection test with the cylinder body should be performed. Otherwise, the BCSDFs remains the same.

When sampling microfacets from a tilted geometric normal, the projected area as in Eq. (10) is also supposed to change; however, keep a_o^\perp unchanged seems to bring only very slight discrepancy at grazing angles (Fig. 9). Therefore, we only adjust the macronormal itself for simplicity. Since we have completely replaced the macronormal with the mesonormal wherever it appears, they share the same notation ω_m throughout the work, except for the discussion in Section 4.1.1 where a differentiation is needed.

It has been assumed that a scale tilt of α causes the outgoing longitudinal angle of the R lobe to be deflected by 2α [MJC*03]. However, this is only true when $\varphi_i = \varphi_o$. When $|\varphi_i - \varphi_o| \rightarrow \pi$, θ_o converges to $-\theta_i$, the same as without scales. We illustrate this phenomenon in Fig. 4. This also results in a distinctly non-separable contraction of the R lobe at both sides near the grazing angle (see Section 4). To our knowledge, d'Eon et. al [dMH14] are the first to mention and model the dependence of θ_o on $|\varphi_i - \varphi_o|$ in the presence of cuticle scales. However, they mainly focus on deriving the expression for the specular cone in the presence of a scale tilt, then add a cosine-modulated longitudinal width around this specular cone. Such formulation describes this contraction in a phenomenological way, rather than being an explanation of the physical process, thus resulting in a non-separable lobe which is difficult to importance-sample.

3.3. Extending the Model to Elliptical Hair Fibers

Our model does not only work for circular cross-sections; in general, the above idea can be applied to any smooth convex shape. The key changes lie in adjusting the differential surface area element da_m and the projected area in the outgoing direction a_o^\perp . We demonstrate the necessary modifications for elliptical cross-sections, as real hair fibers are often roughly elliptical [BP21; KM17].

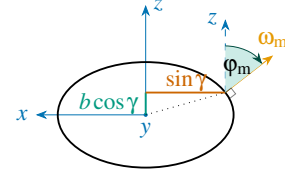


Figure 5: An elliptical cross-section

Assuming the ellipse is parameterized by $x = \sin\gamma, z = b\cos\gamma, \gamma \in [-\pi, \pi]$ (Fig. 5). This gives eccentricity $e = \sqrt{1-b^2}$. The normal vector of a point on the ellipse is $[\sin\varphi, \cos\varphi]^\top$, or $[b\sin\gamma, \cos\gamma]^\top$. da_m in Eqs. (4) and (19) now becomes

$$da_m = \sqrt{1-e^2\sin^2\gamma} d\gamma_m ds, \quad (26)$$

and a_o^\perp in Eq. (10) is replaced by

$$a_o^\perp = 2\sqrt{1-e^2\sin^2\varphi_o} \cos\theta_o ds. \quad (27)$$

After replacing these terms in the above derivation, we arrive at the BCSDF for elliptical fibers

$$S_R(\omega_i, \omega_o) = \frac{R_1}{8\sqrt{1-e^2\sin^2\varphi_o} \cos\theta_o \cos\theta_i} \int D_1 G_1 \sqrt{1-e^2\sin^2\gamma_{m1}} d\gamma_{m1}, \quad (28)$$

$$S_{TT}(\omega_i, \omega_o) = \frac{1}{2\sqrt{1-e^2\sin^2\varphi_o} \cos\theta_o \cos\theta_i} \int \frac{T_1 T_2}{\|\omega_{h1}\|^2 \|\omega_{h2}\|^2} |\omega_i \cdot \omega_{h1}| |\omega_t \cdot \omega_{h1}| |\omega_o \cdot \omega_{h2}| |\omega_t \cdot \omega_{h2}| \int \frac{D_1 D_2 G_1 G_2 A_{tr} \sqrt{1-e^2\sin^2\gamma_{m2}}}{|\omega_t \cdot \omega_{m1}|} d\gamma_{m1} d\omega_t, \quad (29)$$

$$S_{TRT}(\omega_i, \omega_o) = \frac{1}{8\sqrt{1-e^2\sin^2\varphi_o} \cos\theta_o \cos\theta_i} \int \frac{T_1}{\|\omega_{h1}\|^2} |\omega_t \cdot \omega_{h1}| |\omega_i \cdot \omega_{h1}| \int \frac{R_2 T_3}{\|\omega_{h3}\|^2} |\omega_{tr} \cdot \omega_{h3}| |\omega_o \cdot \omega_{h3}| \int \frac{D_1 D_2 D_3 G_1 G_2 G_3 A_{tr} \sqrt{1-e^2\sin^2\gamma_{m3}}}{|\omega_t \cdot \omega_{m1}| |\omega_{tr} \cdot \omega_{m2}|} d\gamma_{m1} d\omega_{tr} d\omega_t. \quad (30)$$

Further, it holds that $\gamma_{m2} = 2\tan^{-1}(b\tan\varphi_t) - \gamma_{m1}$, and $\gamma_{m3} = \gamma_{m1} - 2(\tan^{-1}(b\tan\varphi_t) - \tan^{-1}(b\tan\varphi_{tr})) - \pi$. The attenuation

terms $A_{t, \text{tr}}$ depend on the distance through the medium inside the fiber, which can be obtained by taking the difference between the intersection points divided by $\cos \theta_{t, \text{tr}}$.

Compared to Eqs. (12), (23) and (24), above BCSDFs turn out to have only two additional terms, which is a very minor change.

3.4. Implementation

In this section, we provide the implementation details of our model, including sampling, evaluating the BCSDF and the probability density function (PDF). The code is provided in <https://github.com/RiverInTheSky/roughhair>.

3.4.1. Importance Sampling

Since our model is based on the microfacet theory, the sampling procedure boils down to sampling microfacets at each intersection. For simplicity, we denote the vectors with their spherical coordinates as $\omega_x = \{\theta_x, \phi_x\}$. The importance sampling for circular hair fibers works as follows:

- Randomly select an azimuthal offset h , similar to d'Eon et al. [dMH13].
- Compute the mesonormal $\omega_{m1} = \{\alpha, -\sin^{-1} h\}$, sample a micronormal ω_{h1} , compute the Fresnel reflectance, that is the attenuation of the R lobe $\mathcal{A}_R = R_1$.
- Compute the refracted ray via

$$\omega_t = \frac{1}{\eta} \left(\left(|\omega_i \cdot \omega_{h1}| - \sqrt{\eta^2 + |\omega_i \cdot \omega_{h1}|^2 - 1} \right) \omega_{h1} - \omega_i \right),$$
 compute the mesonormal $\omega_{m2} = \{-\alpha, 2\phi_t - \phi_{m1}\}$ at interface ②, sample a micronormal ω_{h2} , compute the Fresnel reflectance R_2 and the absorption A_t along ω_t . The attenuation of the TT lobe is then $\mathcal{A}_{TT} = T_1 T_2 A_t$, with $T_i = 1 - R_i$.
- Compute the reflected ray via $\omega_{tr} = 2|\omega_i \cdot \omega_{h2}| \omega_{h2} - \omega_t$, compute the mesonormal $\omega_{m3} = \{-\alpha, \phi_{m1} - 2(\phi_t - \phi_{tr}) + \pi\}$, sample a micronormal ω_{h3} , compute the Fresnel transmittance T_3 and the absorption A_{tr} along ω_{tr} . The attenuation of the TRT lobe is then $\mathcal{A}_{TRT} = T_1 R_2 T_3 A_{tr}$.
- Select a lobe with the probability in proportion to the attenuation, compute the outgoing direction of the selected lobe, return sample weight $\mathcal{A}_R + \mathcal{A}_{TT} + \mathcal{A}_{TRT}$, multiplied by the visibility term G in the outgoing direction.

A total of 8 random numbers are needed in this procedure.

3.4.2. BCSDF evaluation

The integration in Eq. (12) can be evaluated either analytically (ignoring the GGX shadowing-masking function, see Section Appendix A) or numerically. For the numerical method, we apply composite Simpson's rule. More sub-intervals are needed when more of the cylinder is visible from both the incoming and the outgoing angles. We found that a step size of 0.7β delivers satisfying results, with β being the GGX or Beckmann roughness. For $\beta = 0.08$, an average of ~ 28 sub-intervals are needed to integrate the R lobe.

Evaluating Eqs. (23) and (24) is trickier, as they involve integration in 3D and 5D, respectively, which is extremely costly to evaluate with deterministic numerical integration methods due to the

curse of dimensionality. We suggest precomputing them and storing the result in a 3D table (4D for elliptical cross-sections), or to apply our proposed combined Monte Carlo-Simpson integration on the fly: That is, for each ϕ_{m1} , we sample an internal path, connect it with the outgoing direction, then compute the integrand along the path, divided by the probability of sampling the internal path.

For the TT lobe, ω_{h1} is sampled, ω_{h2} is computed via $\omega_{h2} = -\omega_t + \omega_o/\eta$. If we importance-sample visible microfacets [Hd14], then Eq. (23) is evaluated as

$$S_{TT}(\omega_i, \omega_o) \approx \frac{1}{2 \cos \theta_o \cos \theta_i} \int \frac{T_1 T_2 G_1(\omega_t) D_2 G_2 A_t}{\eta^2 \|\overline{\omega}_{h2}\|^2} \frac{|\omega_i \cdot \omega_{m1}| |\omega_o \cdot \omega_{h2}| |\omega_t \cdot \omega_{h2}|}{|\omega_t \cdot \omega_{m1}|} d\phi_{m1}, \quad (31)$$

with $G_1(\omega_t)$ being the one-sided Smith's shadowing-masking function for direction ω_t at surface normal ω_{m1} .

For the TRT lobe, ω_{h1} and ω_{h2} are sampled, ω_{h3} is computed via $\omega_{h3} = \omega_{tr} + \omega_o/\eta$. Also sampling visible microfacets, Eq. (24) is evaluated as

$$S_{TRT}(\omega_i, \omega_o) \approx \frac{1}{2 \cos \theta_o \cos \theta_i} \int \frac{T_1 R_2 T_3 G_1(\omega_t) G_2(\omega_{tr}) D_3 G_3 A_{tr}}{\eta^2 \|\overline{\omega}_{h3}\|^2} \frac{|\omega_{tr} \cdot \omega_{h3}| |\omega_o \cdot \omega_{h3}| |\omega_i \cdot \omega_{m1}| |\omega_t \cdot \omega_{m2}|}{|\omega_t \cdot \omega_{m1}| |\omega_{tr} \cdot \omega_{m2}|} d\phi_{m1}, \quad (32)$$

with $G_2(\omega_{tr})$ being Smith's shadowing-masking function for direction ω_{tr} when the surface normal is ω_{m2} .

Now Eqs. (31) and (32) integrate in 1D, we can easily evaluate them using the same composite Simpson's rule as before.

The above method is significantly faster than using quadrature on all dimensions, and has a reasonably low noise level even when we only sample one internal path for each ϕ_m every time the BCSDF is evaluated (Fig. 6). During render time, the function will be evaluated multiple times and gradually converge. In practice, we do not observe more variance in the method than that of d'Eon et al. [dMH13].

3.4.3. Probability Distribution Function

Evaluating the PDF is similar to evaluating the BCSDF, we also integrate along the azimuth. After selecting an azimuthal offset, we sample an internal path (when applicable), compute the attenuation \mathcal{A} of each lobe, and take $\mathcal{A}/\mathcal{A}_R + \mathcal{A}_{TT} + \mathcal{A}_{TRT}$ as an estimate of the probability of sampling a specific lobe; then for each lobe, we multiply $\mathcal{A}/\mathcal{A}_R + \mathcal{A}_{TT} + \mathcal{A}_{TRT}$ by the conditional probability of sampling the final outgoing direction, given that we have sampled the internal path (when applicable). To summarize, the probability of sampling an outgoing direction ω_o given incident direction ω_i is

$$P_{\omega_i}(\omega_o) \approx \frac{1}{2} \int_{-1}^1 \frac{1}{\mathcal{A}_R + \mathcal{A}_{TT} + \mathcal{A}_{TRT}} \left(\frac{\mathcal{A}_R D_1 G_1(\omega_i)}{4 |\omega_i \cdot \omega_{m1}|} + \frac{\mathcal{A}_{TT} D_2 G_2(\omega_t) |\omega_t \cdot \omega_{h2}| |\omega_o \cdot \omega_{h2}|}{\eta^2 \|\overline{\omega}_{h2}\|^2 |\omega_t \cdot \omega_{m2}|} + \frac{\mathcal{A}_{TRT} D_3 G_3(\omega_{tr}) |\omega_{tr} \cdot \omega_{h3}| |\omega_o \cdot \omega_{h3}|}{\eta^2 \|\overline{\omega}_{h3}\|^2 |\omega_{tr} \cdot \omega_{m3}|} \right) dh, \quad (33)$$

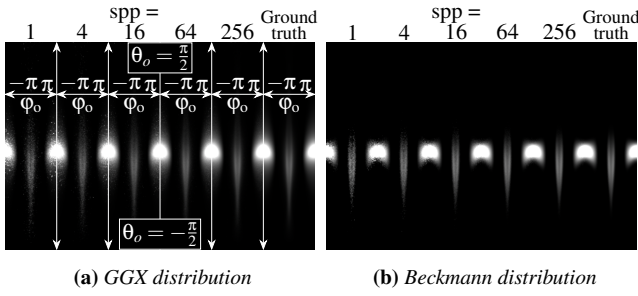


Figure 6: Evaluating $S_{TT} + S_{TRT}$ as a function of θ_o and ϕ_o , with $\theta_i = \phi_i = 0, \sigma_a = 0$ and $\alpha = 4^\circ$. We test our combined Monte Carlo-Simpson integration method with 1, 4, 16, 64, and 256 samples per pixel. The ground truth is computed with Simpson’s rule applied along ϕ_m and Lebedev quadrature [LL99; Bur10] in ω_i and ω_{tr} . In both subfigures $\beta = 0.08$. In Section 4.1 we will explain how such images are produced.

assuming we sample visible normals.

4. Results and Comparison

In this section, we validate our BCSCDF against the ground truth Monte Carlo simulation, and compare both to previous separable [dFH*11] and non-separable [dMH14] models. We also show the final rendering results generated using our and the separable model.

4.1. Validation

Similar to previous non-separable model by d’Eon et al. [dMH14], we run a series of Monte Carlo simulation and compare the results with that computed by Eqs. (12), (23) and (24), as well as the implementation in previous works [dFH*11; dMH14]. For circular cross-section, we keep the azimuthal illumination angle ϕ_i to be 0, and only vary θ_i . In each subfigure in Figs. 7 and 9 to 11, $S(\omega_i, \omega_o) \cos \theta_i$ is plotted in (θ_o, ϕ_o) coordinates. The hair is represented by a rough cylinder made of keratin ($n_{\text{keratin}}/n_{\text{air}} \approx 1.548$), with microfacet roughness and Smith shadowing. We implement a spherical camera in Mitsuba 2 [NVZJ19] that looks at the hair at the sphere center from all directions. The emitter is directional with irradiance 1, the developed film has a resolution of 400×100 . All images are rendered using the `scalar_spectral` variant on an Apple M1 8-core CPU.

Monte Carlo simulation. For each sample on the image pixel, we generate a uniform random offset $h \in [-1, 1]$ on the hair, and perform path tracing towards the emitter. Scale tilt is simulated by centering the normal distribution around the tilted mesonormal, but keeping the local shading frame unchanged. 1024 samples per pixel (spp) are used in Fig. 7 for the R lobe, others with TT and TRT lobes have 65536 spp.

Numerical integration. For each pixel, $S(\omega_i, \omega_o) \cos \theta_i$ is evaluated directly via composite Simpson’s rule or combined numerical method as described in Section 3.4.2.

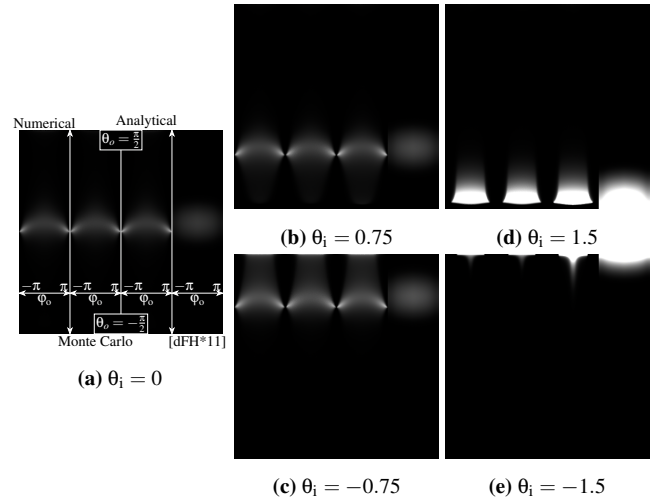


Figure 7: Each subfigure compares the R lobe of four different fiber BCSCDFs, under various illumination angles θ_i . $\alpha = 4^\circ, \text{GGX } \beta = 0.08, \beta_R = 7.7^\circ$. Each image is organized in four stripes: **left:** numerical integration of the proposed model, including the shadowing-masking function G ; **middle left:** ground truth Monte Carlo simulation; **middle right:** analytical integration of the proposed model, excluding G ; **right:** [dFH*11].

Analytical integration without shadowing-masking. There exists an analytical solution for the R lobe with the GGX distribution. $\frac{R_1}{8 \cos \theta_o} \int D d\phi_{m1}$ is evaluated as described in Appendix A.

Previous separable model. We take the implementation of d’Eon et al. [dFH*11; dMH13] with corrected absorption term as stated in Section 3.1.2. Their longitudinal width β_R is not equivalent to our microfacet roughness β ; for comparison, we manually choose a longitudinal width for each microfacet roughness value so that the two deliver approximately the same reflectance of the R lobe at $\theta_i = 0, \theta_o = 0, \phi_o = 0, \alpha = 0$. Such a roughness pair gives almost the same longitudinal span. This choice holds for all such comparisons between our and the separable model [dFH*11].

Previous non-separable model. In Fig. 8, we directly compare with the lat-long images by d’Eon et al. [dMH14]. Their image intensity seems different than ours; therefore, we applied a cosine scaling on our rendered images for a fair comparison, i.e. $S(\omega_i, \omega_o) \cos \theta_i \cos \theta_o$ instead of $S(\omega_i, \omega_o) \cos \theta_i$.

4.1.1. R Lobe of a Circular Cross-Section

Since d’Eon et al.’s model [dMH14] is designed to match Beckmann roughness, we compare the R lobe of the first four aforementioned methods in Fig. 7 with GGX roughness and compare with d’Eon et al.’s work [dMH14] separately with Beckmann roughness in Fig. 8.

In Fig. 7, the numerical solution matches the ground truth Monte Carlo simulation perfectly, even at grazing θ_o angles. The analytical solution also reproduces the ground truth accurately, despite being brighter at extreme grazing θ_o angles, where G should have

been low. By ignoring G we omit the energy loss which comes from visibility inside the microsurface.

The most noticeable difference between the three microfacet-based methods and the separable model lies in the focusing and increased brightness at grazing φ_o angles, as predicted in Fig. 4. The support of the bright lobe does not touch $\varphi_o = \pm\pi$ except when $\theta_i = 0$. Therefore, we are particularly interested in the behavior as φ_o approaches $\pm\pi$. In this case, assuming no scale tilt for the moment, the incoming, outgoing and micronormal angles are

$$\omega_i = \begin{bmatrix} 0 \\ \sin \theta_i \\ \cos \theta_i \end{bmatrix}, \omega_o = \begin{bmatrix} 0 \\ \sin \theta_o \\ -\cos \theta_o \end{bmatrix}, \omega_h = \begin{bmatrix} \sin \varphi_h \cos \theta_h \\ \sin \theta_h \\ \cos \varphi_h \cos \theta_h \end{bmatrix}, \quad (34)$$

respectively. ω_i and ω_o should be visible from the macronormal

$$\omega_m = [\sin \varphi_m, 0, \cos \varphi_m]^\top, \quad (35)$$

therefore,

$$\begin{aligned} \omega_i \cdot \omega_m \geq 0, \omega_o \cdot \omega_m \geq 0 &\Rightarrow \cos \theta_i \cos \varphi_m \geq 0, \cos \theta_o \cos \varphi_m \leq 0 \\ &\Rightarrow \cos \varphi_m = 0 \\ &\Rightarrow \omega_m = [\pm 1, 0, 0]^\top. \end{aligned} \quad (36)$$

It also holds that

$$\begin{aligned} \omega_o &= 2(\omega_i \cdot \omega_h)\omega_h - \omega_i \\ &= 2(\omega_i \cdot \omega_h) \begin{bmatrix} \sin \varphi_h \cos \theta_h \\ \sin \theta_h \\ \cos \varphi_h \cos \theta_h \end{bmatrix} - \begin{bmatrix} 0 \\ \sin \theta_i \\ \cos \theta_i \end{bmatrix}. \end{aligned} \quad (37)$$

Comparing with the expression of ω_o in Eq. (34), it must be either $\sin \varphi_h \cos \theta_h = 0$ or $(\omega_i \cdot \omega_h) = 0$. Assuming $\sin \varphi_h \cos \theta_h = 0$, then $\omega_h = [0, \sin \theta_h, \cos \varphi_h \cos \theta_h]^\top$. From Eq. (36) follows that $\omega_m \cdot \omega_h = 0$; in this case, the normal distribution function $D(\omega_h)$ is extremely low. Therefore, $(\omega_i \cdot \omega_h) = 0$ is a more probable situation. From Eq. (37) we conclude that

$$\omega_o = -[0, \sin \theta_i, \cos \theta_i]^\top. \quad (38)$$

This explains why as $\varphi_o \rightarrow \pm\pi$, the reflection is focused on one point, the longitudinal angle of which is $\theta_o = -\theta_i$.

However, in the presence of tilted surface scales, the incoming and outgoing angles must also be visible from the mesonormal

$$\omega_{m\alpha} = [\sin \varphi_m \cos \alpha, \sin \alpha, \cos \varphi_m \cos \alpha]^\top, \quad (39)$$

therefore

$$\begin{aligned} \omega_i \cdot \omega_{m\alpha} \geq 0, \quad \omega_o \cdot \omega_{m\alpha} \geq 0, \quad \omega_i \cdot \omega_m \geq 0, \quad \omega_o \cdot \omega_m \geq 0 \\ \Rightarrow \cos \varphi_m = -\tan \theta_i \tan \alpha = 0. \end{aligned} \quad (40)$$

When $\alpha \neq 0$, above equation is only satisfied at $\theta_i = 0$. Therefore, at oblique θ_i angles, $\varphi_o = \pm\pi$ is unreachable.

We believe that this focusing and increased brightness at both ends is what Khungurn and Marschner [KM17] described as the *E mode*. According to their measurement and description, the *E mode* “is the brightest around forward directions and is very sharp in the θ_o direction”, and it satisfies “ $\theta_o = -\theta_i$ ”; these observations agree well with the appearance in Fig. 7 as $|\varphi_o| \rightarrow \pi$. Most importantly, this *E mode* is also present in black hairs, indicating that it is caused by reflection. Therefore, we conclude that the *E mode*, instead of

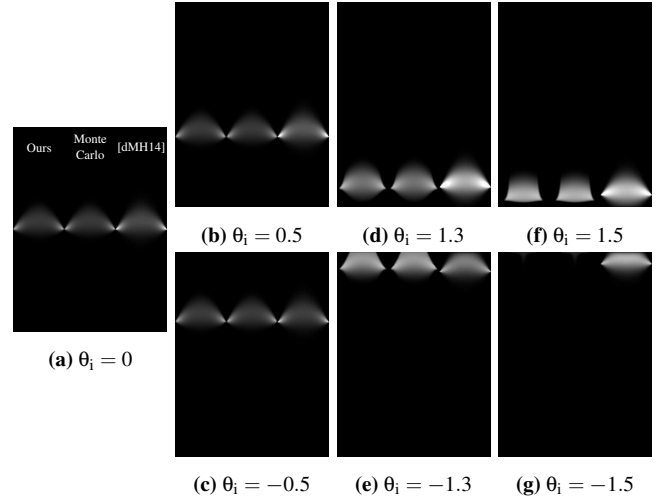


Figure 8: Each subfigure compares the R lobe of three different fiber BCSDFs, under various illumination angles θ_i . $\alpha = 4^\circ$, Beckmann $\beta = 0.08$. Each subfigure is organized in three stripes: **left:** our proposed model with numerical integration; **middle:** ground truth Monte Carlo simulation; **right:** [dMH14].

being a separate mode, is a component of the R mode as a natural result of surface roughness at grazing angles.

In contrast to our method which is completely microfacet-based, previous separable model [dMH14] applies only a cosine modulation in the longitudinal scattering direction based on the separable method [dFH*11]. This approximation matches the Monte Carlo rendering at small inclinations. However, as θ_i gets larger, the focusing brightness in the forward scattering direction can not be described by a cosine modulation anymore, whereas our method still matches the Monte Carlo simulation faithfully (Fig. 8).

4.1.2. TT and TRT Lobes of a Circular Cross-Section

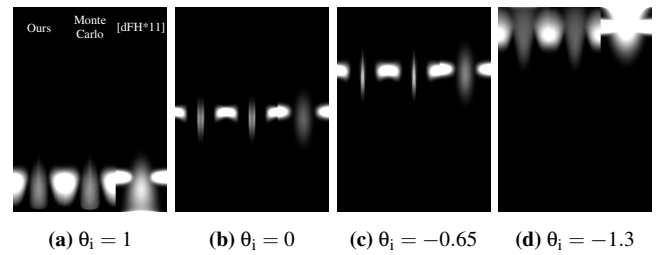


Figure 9: TT plus TRT lobe for various illumination angles θ_i . $\alpha = 2^\circ$, $\sigma_a = 0$, Beckmann $\beta = 0.05$, $\beta_R = 4.4^\circ$. In each subfigure, **left:** Our model evaluated using combined numerical integration as described in Section 3.4.2; **middle:** ground truth Monte Carlo simulation, using 65536 spp; **right:** [dFH*11].

The same comparison as in the previous subsection (without analytical method and non-separable model [dMH14]) is shown in Fig. 9. As before, our model matches the Monte Carlo simulation closely.

Despite the similar longitudinal span, our TRT lobe is more concentrated in the azimuth as compared to the separable model; ours is also less shiny at grazing angles. Furthermore, the two methods have similar TT lobes except at grazing angles. However, this similarity with the previous method only holds for Beckmann roughness as we have used in Fig. 9. GGX roughness has longer tails in the distribution (Fig. 6a) and is hardly comparable with the previous method.

4.1.3. Scattering from Elliptical Fibers

We verify our BCSDF against Monte Carlo simulation in Fig. 10, as we did for the cylindrical fibers. Here, our model also agrees well with the ground truth. The small discrepancy at grazing angles for $\theta_i = 0.7$ might be because that the macro/mesonormal in the Monte Carlo simulation and our theoretical model don't always agree, as mentioned in Section 3.2.

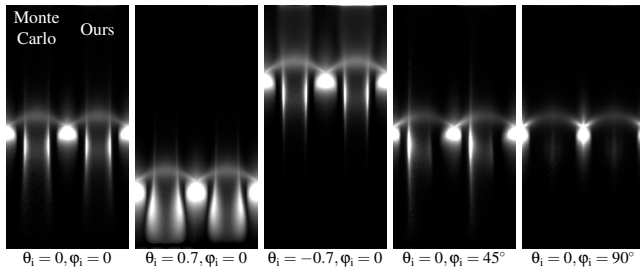


Figure 10: Validating our BCSDF of elliptical cross-section against Monte Carlo simulation, under various illumination angles. $\alpha = 4^\circ$, $\sigma_a = 0$, $\beta = 0.05$, ellipse eccentricity $e = 0.8$. For each of the five pairs: *left*: Monte Carlo simulation of scattering from an elliptical cylinder. *right*: our BCSDF for elliptical cross-section.

We also show the effect of elliptical cross-sections with varying eccentricity on the cosine scaled BCSDF in Fig. 11.

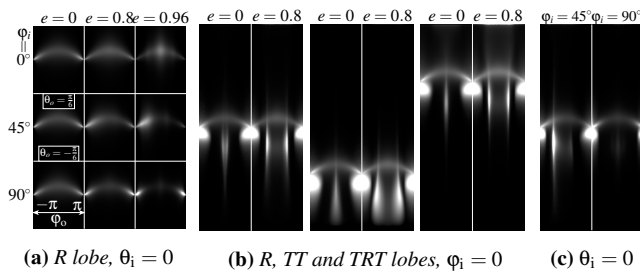


Figure 11: Comparing fiber scattering function of circular and elliptical cross-sections. $\alpha = 4^\circ$, $\sigma_a = 0$, $\beta = 0.05$. (a) R lobe of fibers with various illumination angles in φ_i and different eccentricity e . (b) R, TT and TRT lobes of circular and elliptical fibers with various illumination angles in θ_i . *Left*: $\theta_i = 0$. *Middle*: $\theta_i = 0.7$. *Right*: $\theta_i = -0.7$. (c) R, TT and TRT lobes of a fiber with elliptical cross-section ($e = 0.8$) under oblique illumination angles in φ_i .

The first column in Fig. 11a shows the R lobe for a circular fiber under various illumination angles in φ_i . As expected, the function

is invariant to φ_i due to rotational symmetry. The last column in Fig. 11a shows the R lobe for an elliptical fiber with eccentricity $e = 0.96$. Such an elliptical fiber has a higher value of the *normal distribution function* (NDF) near the z axis than near the x axis (Fig. 5); thus, when the illumination is along the negative z axis ($\varphi_i = 0^\circ$), the reflectance is higher at $\varphi_o = 0$, and lower in the forward scattering direction, compared to a circular fiber. When the illumination is along the negative x axis ($\varphi_i = 90^\circ$), although the NDF is the smallest in the backward scattering direction, the diameter is also the smallest, thus, a locally maximal reflectance is visible at $\varphi_o = 0$. The highest value of the NDF along the z axis and the smallest projected area along the x axis lead to a global maximum in reflectance along the forward scattering function. When $\varphi_i = 45^\circ$, the reflectance has a highest value at around $\varphi_o = -90^\circ$.

An eccentricity of 0.96 is mainly for the purpose of illustrating the above properties. According to Khungurn and Marschner [KM17], a hair fiber has an eccentricity of up to 0.8, which is demonstrated in the middle column of Fig. 11a. There, the above-mentioned properties still hold, but are less significant, especially when compared to the influence of eccentricity on the TRT component in Figs. 11b and 11c. There exists two symmetric extrema for the TRT lobe [MJC*03]. However, for a fiber with an elliptical cross-section, these two extrema are further separated from each other, as is shown in Fig. 11b, left. At oblique θ_i angles (Fig. 11b middle and right pairs), the two extrema of a circular fiber are almost indistinguishable, whereas for an elliptical fiber they are still clearly separated from each other. They also appear to be much brighter than that of a circular fiber. When $\varphi_i = 45^\circ$ (Fig. 11c), the extremum on the left is much brighter than the extremum on the right, similar to what we have discussed before for the R lobe in Fig. 11a. When $\varphi_i = 90^\circ$, the two extrema seem to be merging into one, and the intensity is also much lower, since total internal reflection is less pronounced.

4.2. Rendering Hair Scenes

In this subsection, we render a set of hair scenes to compare our method with the separable model, as well as demonstrate the influence of the absorption and the roughness parameter. The hair and the woman model is taken from Yuksel's website [Yuk20]. For hair with elliptical cross-sections, the semi-minor axis is aligned with the curvature vector.

4.2.1. Circular Cross-Sections

Frontlit. Fig. 12 shows the park scene with strong sunlight right behind the camera. The images are rendered in 600×600 resolution with 1024 spp, accompanied by visualizations of the corresponding BCSDF with $\theta_i = 0$, and the difference images.

One prominent difference between our and the previous separable model lies in the specular highlight at the top of the head. Dark hairs rendered with the Marschner model are almost completely black at the top, whereas ours show more realistic specular highlight at such grazing angles. Another difference is that the Marschner model has broader TRT lobes in the azimuth, causing the same energy to spread in a larger angle; as a result, their model looks more saturated, while ours show higher contrast. Our hair has

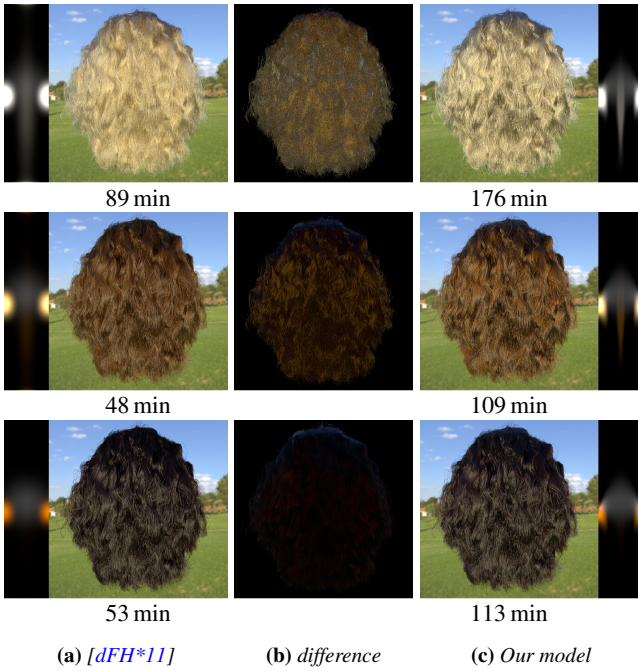


Figure 12: the Park Scene with increasing melanin concentration from top to bottom. $\alpha = -4^\circ$. (a) Marschner model with $\beta_R = 11^\circ$. (c) our model with Beckmann roughness $\beta = 0.135$. (b) the difference between the images on the left and the right side. The exposure value of the accompanying BCSDF visualization is increased by 1 to make the R lobe better visible.

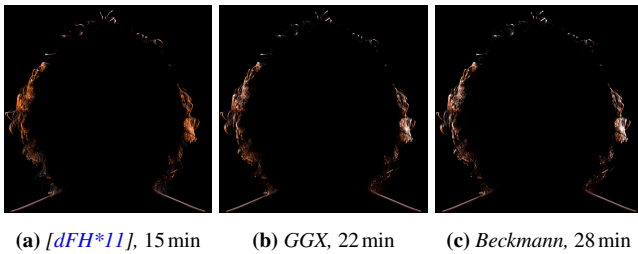


Figure 13: Backlit on dark hairs modelled by previous method and our method, with either Beckmann or GGX roughness. Our method (b,c) produces more realistic images due to the focused forward scattering of the R lobe. All images are rendered with 256 spp. $\alpha = 4^\circ$, $\beta = 0.15$, $\beta_R = 12^\circ$.

a few darker regions in the hair due to occluded highlights, while Marschner’s model spreads the reflectance more uniformly around the occluding fibers. This property is clearly visible in the blond hair. All in all, we found that the Marschner model appears flatter.

Backlit. To demonstrate the glints of the R lobe in the forward scattering direction, we render a studio scene with a small but strong area light source in front of a woman’s head (Figs. 1 and 13).

With the previous method, the forward scattering is dominated by the TT lobe. The R lobe has only very dim response, causing

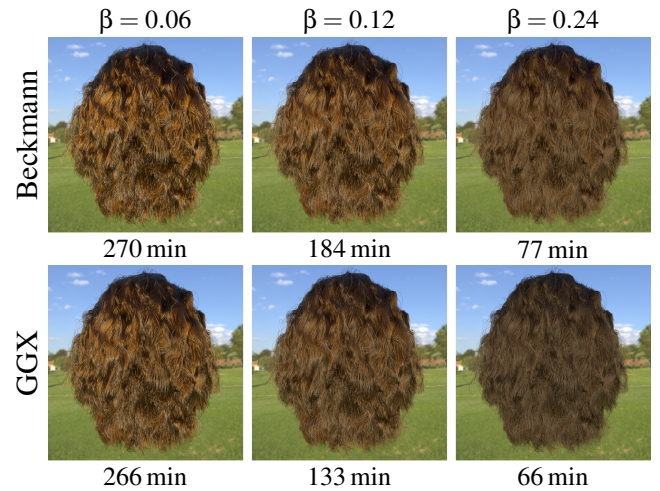


Figure 14: Hair with various roughness. All images are rendered in 600×600 resolution with 1024 spp. $\alpha = 3^\circ$.

the hair to look brown everywhere. With our method, there is a strong highlight due to the R lobe. Such variation in intensity gives the hair more sense of depth.

Roughness. Rougher hairs appear softer (Fig. 14), and take less time to render because of our roughness-dependent integration step size. From Fig. 6 we know that GGX has longer tails in the longitudinal direction; the images therefore also appear softer than those produced by the same Beckmann roughness. A Beckmann roughness of 0.06 to 0.24 is comparable with a Marschner longitudinal width of about 5° to 19° .

4.2.2. Elliptical Cross-Sections

All the renderings in this section are without the PDF computation.

As shown in Fig. 15, the highlight positions from circular and elliptical cross-sections differ significantly. When the illumination angle is perpendicular to the camera plane, the TRT component of the circular cross-section is strong, the hair therefore appears bright; for elliptical cross-sections, however, the TRT component is stronger at oblique illumination angles.

5. Discussion and Limitation

Performance. All the rendered images in Section 4 are annotated with rendering time. As both our and the previous method integrate along the azimuth, we have hoped for a similar rendering time. However, ours are about $1.2 \sim 5 \times$ slower than the previous method. We found out that 60% of the rendering time is spent on computing the PDF, since the PDF is evaluated both for emitter and BSDF sampling using the `path` integrator in Mitsuba 2. This computation time could almost completely be removed by using a cheap approximation of the PDF as a proxy for the weight computation in multiple importance sampling, as is common practice for complex material models. Indeed, as we have dropped the PDF computation completely in Fig. 15, our method shows comparable performance

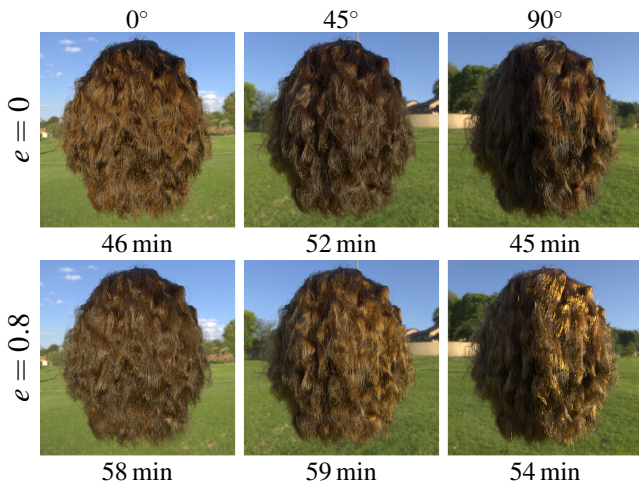


Figure 15: Circular and elliptical hairs under various illumination angles. *Left:* illumination angle perpendicular to the camera plane; *middle:* illumination angle 45° to the camera plane; *right:* illumination angle parallel to the camera plane. Images rendered in 600×600 resolution with 1024 spp. $\alpha = 3^\circ$, Beckmann $\beta = 0.135$.

to the previous method. Rendering elliptical cross-sections takes longer than circular cross-sections because of the extra computation of arc lengths.

Sampling microfacets inside the integration is also expensive: $1/3$ of the total rendering time is spent on sampling microfacets. The numerical evaluation of the R lobe, where no microfacet sampling is performed, takes only 8% of the BCSDf evaluation time.

Since we adjust the integration step size according to the roughness, the rendering time also depends on the roughness. As can be seen in Fig. 14, rough hairs have comparable rendering time as previous work [dMH13]. Production rendering systems would often use a kind of regularization for indirect lighting and use rougher variants of the materials for higher-order scattering. This approach will directly profit from those performance gains.

Energy loss. Our model is based on the assumption that lobes beyond TRT can be ignored due to the little energy they carry. We therefore evaluate the energy loss resulting from this simplification using Monte Carlo simulation.

In the first row of Fig. 16, we show the BCSDf slices of tracing only the first three lobes (R, TT, TRT), tracing lobes beyond the first three, and tracing infinite lobes with zero internal absorption, respectively; in the second row, we show only the lobes beyond the first three with increasing absorption, the same as used in the renderings in Fig. 12.

Fig. 16 shows that lobes beyond TRT are only dimly visible with low internal absorption (blond hair), especially at grazing incident angles. The TRRT lobe still has characteristic shapes, and can be added to the model similarly as described in Section 3, if necessary. Lobes beyond TRRT are very weak and have only low-frequency features; if energy conservation is desired, this contribution can be approximated using a single lobe following Chiang

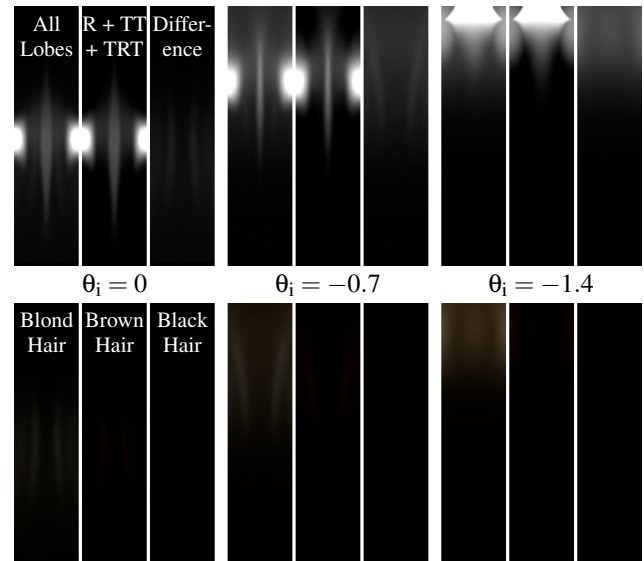


Figure 16: Evaluating high-order lobes for various internal absorption under different incident angles in θ_i using Monte Carlo simulation. $\alpha = 2^\circ$, Beckmann $\beta = 0.15$, $e = 0$. **First row:** $\sigma_\alpha = 0$; for blond, brown, and black hairs, the eumelanin and pheomelanin concentrations $\rho = 0.06, 0.6$, and 1.8 , respectively.

et al. [CBTB16]. For brown and black hairs, the contribution of higher-order lobes is negligible.

Far-field model. We have proposed a far-field scattering model that requires expensive integration along the azimuth; this integration can potentially be skipped to enable near-field scattering [CBTB16].

Wave-optics effect. Our model is a pure geometry one and ignores the wave-optics effect. However, the mean diameter of human hair is $80 \mu\text{m}$ [DK04], at which scale diffraction is present. It would be interesting to trace complex rays with our method, similar to Benamira and Pattanaik's method [BP21].

6. Conclusion and Future Work

In this paper, we present the first microfacet-based hair scattering model. Instead of separating the scattering function in the outgoing direction without physical justification, we model the roughness as a distribution of micronormals and derive a fiber BSDF following well-established microfacet theory. The importance sampling procedure is naturally composed of sampling microfacets. We verify that our R lobe can model the narrow and bright reflectance in the forward scattering direction as observed in previous works. Our R lobe is efficient to evaluate and can find its application in any kind of fibers, including furs with complicated internal scattering. The TT and TRT lobes are restricted to homogenous materials and are slower to evaluate than the previous model due to the high dimensional integration; we are looking forward to a more efficient evaluation method, for example dynamically adjusted subinterval for numerical integration, skipping azimuthal roughness completely so

that no integration is needed, or a new microfacet distribution for which an analytical solution exists. We also demonstrate scattering from elliptical fibers and argue that the model can be extended to any smooth convex shape, which finds its application in fibers with irregular cross-sections [ACG*17].

With this work, we wish to provide a new look at the hair scattering model in a physically-based way.

Acknowledgement

This work was supported by the European Research Council under ERC Starting Grant “ECHO” (802192). Open Access funding enabled and organized by Projekt DEAL.

References

- [ACG*17] ALIAGA, CARLOS, CASTILLO, CARLOS, GUTIERREZ, DIEGO, et al. “An appearance model for textile fibers”. *Computer Graphics Forum*. Vol. 36. 4. Wiley Online Library. 2017, 35–45 12.
- [BP21] BENAMIRA, ALEXIS and PATTANAİK, SUMANTA. “A Combined Scattering and Diffraction Model for Elliptical Hair Rendering”. *Computer Graphics Forum* (2021). ISSN: 1467-8659. DOI: [10.1111/cgfm.14349](https://doi.org/10.1111/cgfm.14349) 2, 5, 11.
- [Bur10] BURKARDT, JOHN. *sphere_lebedev_rule*. 2010. URL: https://people.sc.fsu.edu/~jburkardt/cpp_src/sphere_lebedev_rule/sphere_lebedev_rule.html 7.
- [CBTB16] CHIANG, MATT JEN-YUAN, BITTERLI, BENEDIKT, TAPPAN, CHUCK, and BURLEY, BRENT. “A practical and controllable hair and fur model for production path tracing”. *Computer Graphics Forum*. Vol. 35. 2. Wiley Online Library. 2016, 275–283 2, 11.
- [CT82] COOK, ROBERT L and TORRANCE, KENNETH E. “A reflectance model for computer graphics”. *ACM Transactions on Graphics (TOG)* 1.1 (1982), 7–24. DOI: [10.1145/357290.357293](https://doi.org/10.1145/357290.357293) 2.
- [dFH*11] D’EON, EUGENE, FRANCOIS, GUILLAUME, HILL, MARTIN, et al. “An energy-conserving hair reflectance model”. *Computer Graphics Forum*. Vol. 30. 4. Wiley Online Library. 2011, 1181–1187. DOI: [10.1111/j.1467-8659.2011.01976.x](https://doi.org/10.1111/j.1467-8659.2011.01976.x) 1, 2, 4, 7, 8, 10.
- [DHI*13] DUPUY, JONATHAN, HEITZ, ERIC, IEHL, JEAN-CLAUDE, et al. “Linear Efficient Antialiased Displacement and Reflectance Mapping”. *ACM Transactions on Graphics*. Proceedings of Siggraph Asia 2013 32.6 (Nov. 2013), Article No. 211. DOI: [10.1145/2508363.2508423](https://doi.org/10.1145/2508363.2508423) 3.
- [DJ06] DONNER, CRAIG and JENSEN, HENRIK WANN. “A Spectral BSSRDF for Shading Human Skin.” *Rendering techniques* 2006 (2006), 409–418 4.
- [DK04] DEEDRICK, DOUGLAS W and KOCH, SANDRA L. “Microscopy of Hair Part I: A Practical Guide and Manual for Human Hairs”. *Forensic science communications* 6.1 (2004) 11.
- [dMH13] D’EON, EUGENE, MARSCHNER, STEVE, and HANIKA, JOHANNES. “Importance sampling for physically-based hair fiber models”. *SIGGRAPH Asia 2013 Technical Briefs*. 2013, 1–4. DOI: [10.1145/2542355.2542386](https://doi.org/10.1145/2542355.2542386) 6, 7, 11.
- [dMH14] D’EON, EUGENE, MARSCHNER, STEVE, and HANIKA, JOHANNES. “A fiber scattering model with non-separable lobes”. *ACM SIGGRAPH 2014 Talks*. 2014, 1–1. DOI: [10.1145/2614106.2614161](https://doi.org/10.1145/2614106.2614161) 2, 5, 7, 8.
- [Hd14] HEITZ, ERIC and D’EON, EUGENE. “Importance sampling microfacet-based BSDFs using the distribution of visible normals”. *Computer Graphics Forum*. Vol. 33. 4. Wiley Online Library. 2014, 103–112. DOI: [10.1111/cgfm.12417](https://doi.org/10.1111/cgfm.12417) 6.
- [Hei14] HEITZ, ERIC. “Understanding the Masking-Shadowing Function in Microfacet-Based BRDFs”. *Journal of Computer Graphics Techniques (JCGT)* 3.2 (June 2014), 48–107. ISSN: 2331-7418. URL: <http://jcgt.org/published/0003/02/03/2>.
- [HHdD16] HEITZ, ERIC, HANIKA, JOHANNES, D’EON, EUGENE, and DACHSBACHER, CARSTEN. “Multiple-scattering microfacet BSDFs with the Smith model”. *ACM Transactions on Graphics (TOG)* 35.4 (2016), 1–14 3.
- [KK89] KAJIYA, J. T. and KAY, T. L. “Rendering Fur with Three Dimensional Textures”. *SIGGRAPH Comput. Graph.* 23.3 (July 1989), 271–280. ISSN: 0097-8930. DOI: [10.1145/74334.74361](https://doi.org/10.1145/74334.74361) 1.
- [KM17] KHUNGURN, PRAMOOK and MARSCHNER, STEVE. “Azimuthal scattering from elliptical hair fibers”. *ACM Transactions on Graphics (TOG)* 36.2 (2017), 1–23. DOI: [10.1145/2998578.2998580](https://doi.org/10.1145/2998578.2998580) 2, 5, 8, 9.
- [LJJ*18] LEE, JOO HO, JARABO, ADRIAN, JEON, DANIEL S, et al. “Practical multiple scattering for rough surfaces”. *ACM Transactions on Graphics (TOG)* 37.6 (2018), 1–12 3.
- [LL99] LEBEDEV, VYACHESLAV IVANOVICH and LAIKOV, DN. “A quadrature formula for the sphere of the 131st algebraic order of accuracy”. *Doklady Mathematics*. Vol. 59. 3. Pleiades Publishing, Ltd. 1999, 477–481 7.
- [MJC*03] MARSCHNER, STEPHEN R, JENSEN, HENRIK WANN, CAMMARANO, MIKE, et al. “Light scattering from human hair fibers”. *ACM Transactions on Graphics (TOG)* 22.3 (2003), 780–791. DOI: [10.1145/882262.882345](https://doi.org/10.1145/882262.882345) 1, 2, 4, 5, 9.
- [NVZJ19] NIMIER-DAVID, MERLIN, VICINI, DELIO, ZELTNER, TIZIAN, and JAKOB, WENZEL. “Mitsuba 2: A Retargetable Forward and Inverse Renderer”. *Transactions on Graphics (Proceedings of SIGGRAPH Asia)* 38.6 (Dec. 2019). DOI: [10.1145/3355089.3356498](https://doi.org/10.1145/3355089.3356498) 7.
- [Pha16] PHARR, MATT. *The Implementation of a Hair Scattering Model*. 2016. URL: <https://www.pbrt.org/hair.pdf> 4.
- [PJH18] PHARR, MATT, JAKOB, WENZEL, and HUMPHREYS, GREG. *Physically based rendering: From theory to implementation*. 3rd ed. Morgan Kaufmann, 2018. URL: <https://www.pbr-book.org/3ed-2018> 2.
- [SHHD17] SCHÜSSLER, VINCENT, HEITZ, ERIC, HANIKA, JOHANNES, and DACHSBACHER, CARSTEN. “Microfacet-based Normal Mapping for Robust Monte Carlo Path Tracing”. *Transactions on Graphics (Proceedings of SIGGRAPH Asia)* 36.6 (Nov. 2017), 205:1–205:12. DOI: [10.1145/3130800.3130806](https://doi.org/10.1145/3130800.3130806) 3.
- [Smi67] SMITH, BRUCE. “Geometrical shadowing of a random rough surface”. *IEEE transactions on antennas and propagation* 15.5 (1967), 668–671. DOI: [10.1109/TAP.1967.1138991](https://doi.org/10.1109/TAP.1967.1138991) 2.
- [Tur19] TURQUIN, EMMANUEL. “Practical multiple scattering compensation for microfacet models”. URL: https://blog.selfshadow.com/publications/turquin/ms_comp_final.pdf 45 (2019) 3.
- [XWM*20] XIA, MENGQI (MANDY), WALTER, BRUCE, MICHIELSSEN, ERIC, et al. “A Wave Optics Based Fiber Scattering Model”. *ACM Trans. Graph.* 39.6 (2020). ISSN: 0730-0301. DOI: [10.1145/3414685.3417841](https://doi.org/10.1145/3414685.3417841) 2.
- [YJR17] YAN, LING-QI, JENSEN, HENRIK WANN, and RAMAMOORTHY, RAVI. “An efficient and practical near and far field fur reflectance model”. *ACM Transactions on Graphics (TOG)* 36.4 (2017), 1–13. DOI: [10.1145/3072959.3073600](https://doi.org/10.1145/3072959.3073600) 2, 4.
- [YTJR15] YAN, LING-QI, TSENG, CHI-WEI, JENSEN, HENRIK WANN, and RAMAMOORTHY, RAVI. “Physically-accurate fur reflectance: Modeling, measurement and rendering”. *ACM Transactions on Graphics (TOG)* 34.6 (2015), 1–13. DOI: [10.1145/2816795.2818080](https://doi.org/10.1145/2816795.2818080) 2, 4.
- [Yuk20] YUKSEL, CEM. *HAIR Model Files*. 2020. URL: www.cemyuksel.com/research/hairmodels9.

Appendix A. Analytical Integration of the R lobe for GGX

The GGX distribution with roughness parameter β is

$$D(\omega_h, \omega_m) = \frac{\beta^2}{\pi(1 + (\beta^2 - 1)(\omega_h \cdot \omega_m)^2)^2}, \quad (41)$$

where

$$\begin{aligned} \omega_h \cdot \omega_m \alpha &= \sin \varphi_h \cos \theta_h \sin \varphi_m \cos \alpha + \sin \theta_h \sin \alpha \\ &+ \cos \varphi_h \cos \theta_h \cos \varphi_m \cos \alpha \\ &= \cos \theta_h \cos \alpha \cos(\varphi_h - \varphi_m) + \sin \theta_h \sin \alpha. \end{aligned} \quad (42)$$

Substituting $\cos \theta_h \cos \alpha \sqrt{1 - \beta^2}$ with A , $\sin \theta_h \sin \alpha \sqrt{1 - \beta^2}$ with B , the indefinite integral of Eq. (41) in φ_m is then

$$\begin{aligned} \int D(\omega_h, \omega_m \alpha) d\varphi_m &= \frac{\beta^2}{\pi} \int \frac{1}{(1 - (A \cos(\varphi_h - \varphi_m) + B)^2)^2} d\varphi_m \\ &= \frac{\beta^2}{4\pi} \left(\frac{2(A^2 - B^2 + 3B - 2)}{((B - 1)^2 - A^2)^{3/2}} \tan^{-1} \left(\frac{(A - B + 1) \tan \frac{\varphi_h - \varphi_m}{2}}{\sqrt{(B - 1)^2 - A^2}} \right) + \right. \\ &\quad \frac{2(A^2 - B^2 - 3B - 2)}{((B + 1)^2 - A^2)^{3/2}} \tan^{-1} \left(\frac{(B - A + 1) \tan \frac{\varphi_h - \varphi_m}{2}}{\sqrt{(B + 1)^2 - A^2}} \right) + \\ &\quad \left. \frac{A \sin(\varphi_h - \varphi_m)}{((B - 1)^2 - A^2) (A \cos(\varphi_h - \varphi_m) + B - 1)} + \right. \\ &\quad \left. \frac{A \sin(\varphi_h - \varphi_m)}{((B + 1)^2 - A^2) (A \cos(\varphi_h - \varphi_m) + B + 1)} \right) + C, \end{aligned} \quad (43)$$

with C being some constant. If the scale tilt $\alpha = 0$, the above equation can be simplified as

$$\begin{aligned} \int D(\omega_h, \omega_m) d\varphi_m &= \frac{\beta^2}{\pi} \int \frac{1}{(1 - A^2 \cos^2(\varphi_h - \varphi_m))^2} d\varphi_m \\ &= \frac{\beta^2}{2\pi} \left(\frac{(A^2 - 2)}{(1 - A^2)^{3/2}} \tan^{-1} \left(\frac{\tan(\varphi_h - \varphi_m)}{\sqrt{1 - A^2}} \right) + \right. \\ &\quad \left. \frac{A^2 \sin(2(\varphi_h - \varphi_m))}{(1 - A^2)(A^2 \cos(2(\varphi_h - \varphi_m)) + A^2 - 2)} \right) + C. \end{aligned} \quad (44)$$

The lower bound of the integral is the minimal possible φ_m that satisfies $\omega_m \cdot \omega_i > 0$ and $\omega_m \cdot \omega_o > 0$, the upper bound of the integral is likewise the maximal possible φ_m that satisfies the same inequations.